Research Article | Vol. 26, No. 20 | 1 Oct 2018 | OPTICS EXPRESS 26422
Optics EXPRESS

Feedback control for microring weight banks

ALEXANDER N. TAIT,[1,*] HASITHA JAYATILLEKA,[2] THOMAS FERREIRA DE LIMA,[1] PHILIP Y. MA,[1] MITCHELL A. NAHMIAS,[1] BHAVIN J. SHASTRI,[1] SUDIP SHEKHAR,[2] LUKAS CHROSTOWSKI,[2] AND PAUL R. PRUCNAL[1]

[1] *Princeton University, Princeton, NJ, USA*
[2] *University of British Columbia, Vancouver, British Columbia, Canada*
[*] *atait@ieee.org*

Abstract: Microring weight banks present novel opportunities for reconfigurable, high-performance analog signal processing in photonics. Controlling microring filter response is a challenge due to fabrication variations and thermal sensitivity. Prior work showed continuous weight control of multiple wavelength-division multiplexed signals in a bank of microrings based on calibration and feedforward control. Other prior work has shown resonance locking based on feedback control by monitoring photoabsorption-induced changes in resistance across in-ring photoconductive heaters. In this work, we demonstrate continuous, multi-channel control of a microring weight bank with an effective 5.1 bits of accuracy on 2Gbps signals. Unlike resonance locking, the approach relies on an estimate of filter transmission versus photo-induced resistance changes. We introduce an estimate still capable of providing 4.2 bits of accuracy without any direct transmission measurements. Furthermore, we present a detailed characterization of this response for different values of carrier wavelength offset and power. Feedback weight control renders tractable the weight control problem in reconfigurable analog photonic networks.

1. Introduction

The rapid advances in silicon photonics are rooted in demands for datacenter transceivers; however, they will profoundly impact a wide range of other application areas [1]. Microfabrication ecosystems propel technology roadmapping [2], library standardization [3, 4], and broadened accessibility [5], all of which could reinvigorate research into scalable photonic information – not just signal – processing systems. It has long been recognized that the physical properties of optics impose barriers to digital logic [6] yet present unique advantages for analog processing functions. Larger-scale analog optical processors based on field evolution in free-space [7, 8] and holograms [9, 10] have been shown but have so far not widely adopted, in part, because they could not be integrated. Integrated photonic devices have already found analog signal processing niches where electronics can no longer satisfy demands for bandwidth, dynamic range, and reconfigurability, as exemplified in the field of microwave photonics [11, 12]. Many high-performance operations demonstrated so far are relatively simple from a computing standpoint, such as delaying [13, 14], transport [15, 16], and time-frequency transforms [17–19].

In a distinct vein from simply improving the performance of signal processing elements. silicon photonic integration opens fundamentally new opportunities for large-scale analog information processing systems. Silicon photonic devices are substantially more compact and responsive to tuning than other photonic integrated platforms, properties that have been exploited for large, reconfigurable linear systems [20–22]. Recently, there has been a growing interest in neuromorphic photonics [23, 24] – scalable analog systems whose governing physical equations are isomorphic to those describing an abstract neural network model [25–27]. Photonic neural networks could potentially unlock new domains of machine intelligence by combining ultrafast speeds offered by photonics, energy efficiency offered by neuromorphic architectures,

#335465 https://doi.org/10.1364/OE.26.026422
Journal © 2018 Received 18 Jun 2018; revised 21 Jul 2018; accepted 22 Jul 2018; published 26 Sep 2018

Optics EXPRESS

and demonstrated algorithmic strengths of artificial neural networks. An advantage of strict isomorphism to neural models means that we can confidently predict that established algorithmic techniques can be applied, so we can begin to determine the minimum useful scale of initial photonic neural networks. Recurrent networks become useful at significantly smaller scale than deep, feedforward networks since neurons are, in some sense, reused over time. Examples of known tasks and techniques for recurrent networks include robot control through evolutionary optimization [28] (13 neurons), predictive control through quadratic programming [29] (10's of neurons), pattern recognition through reservoir training [30] (16 nodes), and accelerated simulation through differential equation synthesis [25] (25 neurons).

Any potential of photonic neural networks rests squarely on the ability to configure the strength of connections (i.e. the weights) between photonic neurons. The number of weights scales quadratically with the number of neurons. As such, they are the primary source of complexity and configurability in such networks as well as the most demanding technical challenge. A contrasting approach called reservoir computing can avoid the challenge of weight control and has also received recent attention from the photonics community [30–34]. A reservoir is a fixed complex system that can be made to exhibit a desired behavior through instance-specific supervised training. While this means a reservoir cannot be programmed or guaranteed to produce a particular behavior at a particular scale, it does eliminate the need to control many parameters inside of the system.

Microring (MRR) weight banks bring photonic weighted addition to integrated silicon photonic platforms [35]. Inputs are power modulated, wavelength division multiplexed (WDM) optical signals, and the MRR weight bank is a tunable spectral filter. An MRR weight bank, diagrammed in Fig. 1(a), consists of parallel-coupled microrings (i.e. coupled via a pair of bus WGs). Each MRR independently controls the transmission of exactly one of the WDM signals. Balanced photodetection of these weighted, mutually incoherent WDM signals [36] produces an electrical current representing the weighted sum of the original signals.

A critical vulnerability of analog systems is device parameter variations, which corrupt representations of continuous values. Strategies for counteracting variation have been developed for analog electronic coprocessors [37, 38] and neural networks [39]; corresponding strategies must be developed for photonics before the processing potentials of analog photonic networks can be realized. Post-fabrication resonator trimming has been shown to partially counteract static variation caused by fabrication non-idealities in MRRs [40–42]. After reprocessing, these devices are vulnerable to dynamic variability, such as environmental fluctuations. Tunable elements can be used to address dynamic variation while simultaneously reconfiguring to desired states (e.g. on and off resonance). Tunable approaches can separated into two main categories: 1) feedforward control based on calibration of the parameters of interest, and 2) feedback control based on sensing the state of the parameters online. Feedback can eliminate the need to recalibrate every time the environment changes and offers a simplified calibration and modeling requirement. In this article, we report the first photonic weight banks with feedback control capabilities.

MRR weight banks are a key component of the silicon foundry-compatible neuromorphic photonic architecture called broadcast-and-weight [43], recently demonstrated in [25] and diagrammed in Fig. 1(b). In this protocol, photonic neurons modulate unique WDM carriers that are broadcast to all others. Each connection between a pair of neurons is configured by one MRR weight, a given WDM signal passing by the rest of the MRRs in the bank with minimal excess loss. Photonic neurons compatible with broadcast-and-weight are optical-in, optical-out devices that must be able to convert multiple wavelengths to a single wavelength with a nonlinear transfer function. These conditions are both challenging in all-optical devices but are readily met by an OEO chain consisting of a photodetector connected to a laser [44–46] or modulator [25, 47].

MRRs are a promising candidate for reconfigurable weighting because of their ubiquity in silicon photonics, innate WDM compatibility, and small footprints. Outside of analog photonic

Optics EXPRESS

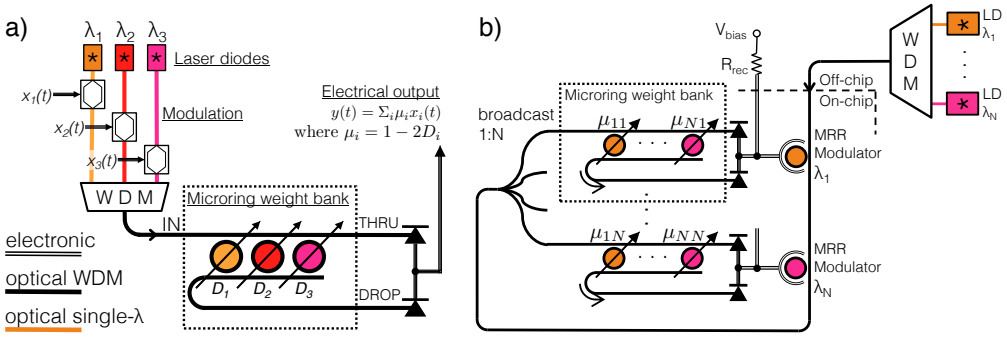

Fig. 1. a) An isolated microring weight bank. Input signals, x_i, are power modulated onto WDM carriers and multiplexed. Each is weighted by one tunable MRR weight, μ_i, whose value is the difference of complementary THRU and DROP port transmissions. A balanced photodetector produces their weighted sum. b) A recurrent silicon photonic broadcast-and-weight network. WDM pumps are multiplexed off-chip and modulated by MRR modulator-class photonic neurons. Connections between neurons are controlled by MRR weights in a square matrix. Balanced photodetectors drive the neurons, which are biased by V_{bias} and R_{rec}.

networks, MRR-based systems have shown relevance to arbitrary waveform generation [17, 19], digital networks [48], directed logic [49], certain reservoir computers [30, 34], and multivariate photonics [50, 51]. The resonant qualities of an MRR lead to sharp dependencies on factors influencing the effective optical path length of the MRR (e.g. temperature, fabrication non-ideality, and semiconductor carrier concentration). This high sensitivity makes them very efficient to tune but especially difficult to control.

Prior work on MRR weight control demonstrated weight control over all WDM channels that was continuous, complementary (range from –1 to +1), independent over channels, and accurate (weight resolution of 4.1 bits + 1 sign bit, i.e. 3% error) [52]. Weight control in these works employed a *feedforward* approach, which has several disadvantages: 1) the calibration phase requires a suite of external measurement equipment, including an optical spectrum analyzer, oscilloscope, and pattern generator, 2) the control rule relies on inverting a model of the device, so that the model must have high fidelity and be precisely calibrated, and 3) the strategy is not robust to temperature fluctuations after the calibration phase. These render the feedforward approach infeasible for all but small-scale situations.

In this work, we demonstrate a feedback weight control approach that 1) requires only one electrical source-meter per MRR, as opposed to an optical probing setup, 2) has a simpler calibration procedure and control model, and 3) is robust to environmental fluctuations in temperature. The feedback weight bank and calibration/control procedures make it practical to control large-scale reconfigurable analog MRR systems such as photonic neural networks. We obtain feedback capabilities by embedding a silicon in-ring photoconductive heater [53] within the waveguide of each MRR weight.

Circulating power sensing using N-doped heaters was introduced by Jayatilleka et al. in [53]. The microring waveguide is lightly doped with donor carriers, forming an in-ring resistor, as shown in Fig. 2(b). Applying current heats the ring thereby shifting the resonance peak. At the same time, a portion of circulating optical power is absorbed, creating electron-hole pairs, which, in turn, increase the conductivity of the heater. By applying current and measuring voltage (or vice verse), the amount of light circulating in the MRR can be sensed. In-ring N-doped photoconductive heaters have been used for automatic resonance locking of more advanced

Optics EXPRESS

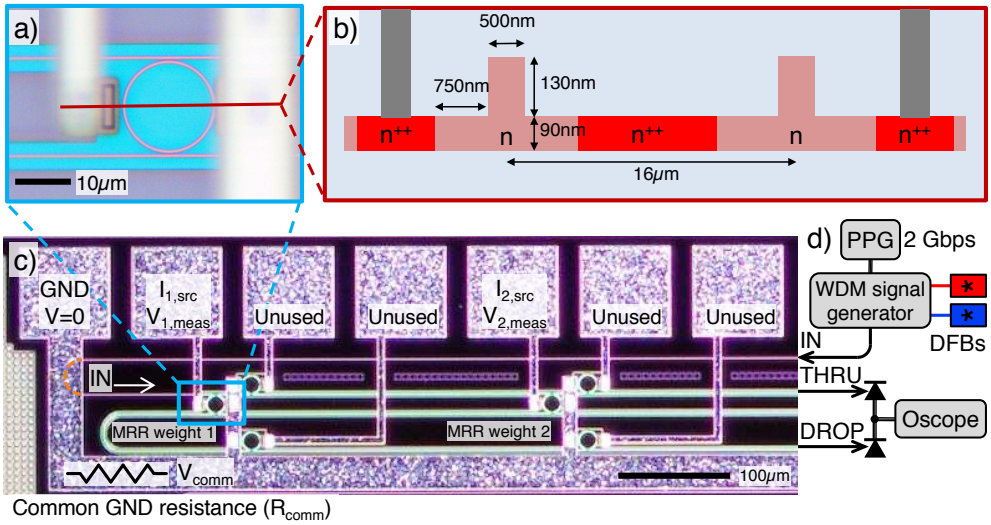

Fig. 2. a) Picture of one N-doped microring. b) Cross section of microring showing etch geometry and dopant pattern. c) Picture of photonic weight bank with two N-doped microring weights. The weight MRRs are tuned by current sources with voltage sense, and other MRRs for sensing are unused. The common voltage is across the parasitic resistance of the common ground connection. d) Experimental setup for generating 1Gbps independently modulated WDM inputs [62]. Weights are measured by a balanced photodiode connected to an oscilloscope.

higher-order MRR filters [54]. Resonance locking and stabilization has also been shown using a variety of in-ring optical sensors [55–57] and external sensors [58, 59]. Prior work centers around tracking a single maximum photoresponse point, corresponding to on-resonance. Feedback control in non-resonant circuits has also been proposed [60] and demonstrated [61] to track a point at which multi-mode input mixtures are demixed into a single mode. In contrast, the goal in this work is to configure over a continuous range of transmission values along the resonance edge.

2. Methods

2.1. Device fabrication

Samples were fabricated on silicon-on-insulator wafers at the IME A*STAR foundry [3]. A cross-section of the N-doped heater within the MRR is shown in Fig. 2(b). Silicon thickness is 220nm, and buried oxide thickness is 2μm. 500nm wide WGs were patterned by deep ultraviolet (DUV) lithography. The WGs used with N doping were etched to a pedestal with 90nm thickness. Following the design of [53], a 2μm wide N-doping section was patterned to follow the MRR WGs, outside of which heavy N^{++} doping is used to make ohmic contacts. Phosphorous dopant concentrations were N: 5×10^{17} and N++: 5×10^{20} cm^{-3} [63]. In a final step, metal vias and traces were deposited to connect the heater contacts to electrical probe pads.

The MRR design, shown in Fig. 2(a), consist of a circular WG with designed radii of 8.000μm and 7.998μm. Coupling region gaps are 250nm, and neighboring MRRs are separated by 300μm. The weight bank device pictured in Fig. 2(c) consists of two bus waveguides and two MRRs in a parallel add/drop configuration, each of which controls a single wavelength channel. Neighboring MRRs are designed with a minuscule 12nm perimeter difference, chosen to create an offset in initial resonance wavelengths of roughly 3nm. The heater contacts on the GND side share a

Optics EXPRESS

common connection to reduce electrical I/O count. Each of the contacts on the opposite side is routed to its own electrical pad. In addition to the parallel-coupled add/drop *weight* MRRs responsible for directing light between the DROP and THRU ports, two more *sense* MRRs were fabricated per channel. These were included as test structures and are not necessary for the calibration procedure developed below.

2.2. Setup

The experimental setup is shown in Fig. 2(d). The sample is mounted on a temperature-controlled alignment stage and coupled to fiber with TE focusing grating couplers [64]. The weight bank DROP and THRU outputs are coupled off chip and detected by a high-speed balanced photodetector (Discovery Semiconductors, Inc. DSC-R405ER), the resulting output recorded by a sampling oscilloscope (Tektronix DSA8300). Each N-doped heater embedded in a MRR is driven by a computer-controlled Keithley 2400 source meter used in current source, voltage sense mode. In contrast to the prior work on MRR weight bank control [52], no optical transmission spectrum analyzer is needed to tune filters onto resonance and assist with model thermal calibration.

Inputs are derived from the multi-wavelength reference input generator, described in more detail in [62]. It produces WDM signals with statistically independent power envelopes by imparting wavelength-dependent delays on a 2Gbps pseudo-random bit sequence (PRBS). Input signal references are recorded and stored by turning each DFB on individually. This setup enables scope-based decomposition of the full weight vector based on the weighted sum. We use $\mathbf{x_i}$ to denote the reference signal of channel i as a vector of sampled points over a set of discrete sampling times. Defining the full input signal basis as, X,

$$X = \begin{bmatrix} x_{1,[t=1]} & x_{2,[t=1]} & \cdots & x_{N,[t=1]} \\ x_{1,[t=2]} & x_{2,[t=2]} & \cdots & x_{N,[t=2]} \\ & \vdots & & \end{bmatrix} \tag{1}$$

$$= [\mathbf{x_1},\ \mathbf{x_2},\ \ldots,\ \mathbf{x_N}] \tag{2}$$

The measured output signal is a weighted sum of these inputs: $\mathbf{y} = X\boldsymbol{\mu}$, where $\boldsymbol{\mu}$ is the weight vector that can have positive and negative values. We use the Moore-Penrose pseudoinverse to decompose the measured output into an estimated weight vector

$$\hat{\boldsymbol{\mu}} = X^{+}\mathbf{y} \tag{3}$$

where $\hat{\boldsymbol{\mu}}$ is the measurement-based estimate of the weight vector, and the psuedoinverse of the input signal basis is $X^{+} = \left(X^{T}X\right)^{-1}X^{T}$. This weight decomposition technique represents an improvement upon the method introduced in the previous work. Prior work required $\mathbf{x_i}$ to be *orthogonal* to all $\mathbf{x_{j\neq i}}$, while, here, the requirement is greatly relaxed from orthogonality to independence.

2.3. Basic characterization

A thermo-electric characterization of the N-doped MRRs is performed using a source-meter. Variables are as defined in the Appendix. First, the stage temperature is varied while resistance is measured at low current, yielding a thermo-electric coefficient of β =3.5Ω/K. The applied current is then swept, measuring voltage, shown in Fig. 3(a)– 3(d) (blue curves). The resistance vs. electrical power is approximately linear with $R_0 = 1.9k\Omega$ and α =134Ω/mW, indicating a self-heating coefficient of z =38.4K/mW. Then, the electrical response is measured in the presence of a strong fixed laser, shown in Fig. 3(a)– 3(d) (red curves). The laser causes a photoresponse resulting in a difference between measured voltage, V, and the baseline (no light)

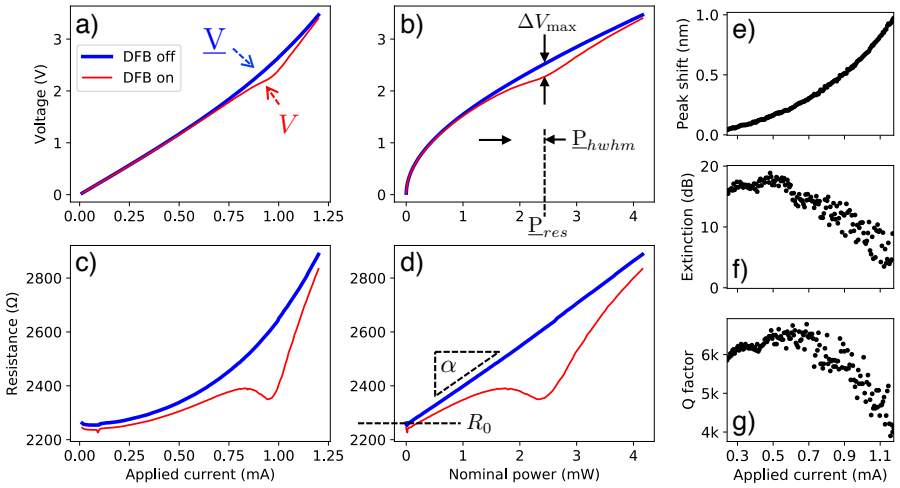

Fig. 3. (a-d) Electrical response to bias current (a, c) and nominal power (b, d) with the DFB laser on (red) and off (blue). Resistance is dependent on temperature changes due to ohmic heating and on the presence of circulating optical power. The meanings of several device and control variables are illustrated. (e-g) Optical properties of the resonator vs. bias. To first order, wavelength shifts (e) are a quadratic function of current. Above a bias of 0.6mA, extinction ratio (f) and Q factor (g) begin to degrade due to additional loss in the heater.

voltage, $\underline{V}$. Fig. 3(b)–3(d) illustrates the control parameters $\Delta V_{\max}$, $\underline{P}_{res}$, $\underline{P}_{hwhm}$, α, and R_0 that are described and used in the next section. Their values are found in Table 1.

Optical and thermo-optic characterization is performed with an optical spectrum analyzer (Apex AP2440A). The radii of the MRRs were designed with 0.2% difference so that their as-fabricated resonances would be unlikely to coincide. Both MRRs have a half-width half maximum of 0.15nm (i.e. Q factor of 5,900). Their resonance peaks, λ_0, fall at 1551.78 and 1553.39nm, respectively. FSR is 12.1nm for both MRRs. The finesse (i.e. FSR / FWHM) is 40.2. Observing the resonance shift vs. applied power in Fig. 3(e), we find the thermo-optic coefficient to be k =6.54pm/K, resulting in thermal tuning efficiency kz = 0.25nm/mW (i.e. 47GHz/mW or 48mW/FSR). Observing the other peak shift, we observe a very small thermal cross-talk ratio of 0.28%. THRU port extinction ratio seen in Fig. 3(f) is level between 0mA to 0.5mA, above which, it falls from 20dB (1%) to 5dB (32%). At high bias on-resonance, at most 68% of light is available at the DROP port, resulting in a minimum insertion loss of 1.7dB. In broadcast and weight, each path of each wavelength interacts with only one MRR weight, so this loss does not cascade in proportion to number of neurons. The knee-like dependence of extinction ratio and Q factor indicates that either the bus-to-ring coupling coefficients or the absorption within the ring are affected by applied electrical power, which is studied more extensively in Sec. 5.

3. Calibration and control procedures

A controller uses actuators and sensors in attempts to set control variables to desired values. A generic feedback control system is diagrammed in Fig. 4. In this case, the actuator is current source, sensor is voltage measurement, and control variable is weight. Within the controller, there is a simplified model of the device, which has parameter values that must be calibrated before evaluation. An evaluator is a procedure that 1) generates command values, 2) directly measures the controlled values of interest, and 3) compares the desired to actual weights.

Optics EXPRESS

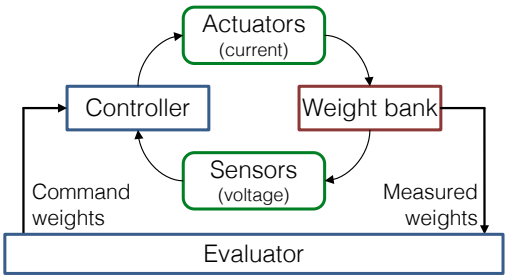

Fig. 4. Concept of feedback control and control evaluation. In feedforward control, there is no sensor path from the device back to the controller.

The control model used in this work, starting from desired weight and ending at applied current, is pictured in Fig. 5(a). It can be summarized as

$$\langle \mu \rangle \rightarrow \langle D \rangle \rightarrow \underbrace{\left\langle \hat{D} \right\rangle \rightarrow \langle \delta \rangle}_{\text{feedback control rule}} \rightarrow \left\langle \underline{\mathrm{P}} \right\rangle \rightarrow \langle I \rangle \tag{4}$$

where the intermediate control variables and rules are described in Table 1. μ is weight, the control variable. D and $\hat{D}$ are, respectively, actual and estimated DROP port transmission. δ and $\underline{\mathrm{P}}$ are, respectively, normalized and nominal electrical power. $\langle I \rangle$ is applied current, the actuation variable. The intermediate conversions (e.g. from current to normalized power shift) are needed to properly scale the feedback search domain. We use $\hat{\cdot}$ notation to denote an estimate, $\langle \cdot \rangle$ to denote a command/desired variable, and $\leftarrow$ to denote assignment, in other words, how to command the left variable in order to satisfy the expression on the right.

Table 1. **Control variables**

Name	Symbol	Equation	Expression	Control rule
Applied current	I			$\langle I \rangle \leftarrow \sqrt{\frac{\langle \underline{\mathrm{P}} \rangle}{R_0(1+\alpha\langle \underline{\mathrm{P}} \rangle)}}$
Nominal electrical power	$\underline{\mathrm{P}}$	(12)	$\frac{I^2 R_0}{1-\alpha I^2 R_0}$	$\left\langle \underline{\mathrm{P}} \right\rangle \leftarrow \underline{\mathrm{P}}_{hwhm} \langle \delta \rangle + \underline{\mathrm{P}}_{res}$
Normalized power	δ	(7)	$\underline{\mathrm{P}}_{hwhm}^{-1}(\underline{\mathrm{P}} - \underline{\mathrm{P}}_{res})$	$\langle \delta \rangle \leftarrow \text{search} - \left\langle \hat{D} \right\rangle$
Estimated transmission	$\hat{D}$	(19)	$\left(\frac{\Delta V}{\Delta V_{\max}}\right)^2$	$\left\langle \hat{D} \right\rangle \leftarrow \hat{g}^{-1}(\langle D \rangle)$
Actual transmission	D			$\langle D \rangle \leftarrow \frac{1-\langle \mu \rangle}{2}$
Weight	μ	(21)	$1 - 2D$	

A key advantage of feedback control is a relaxed modeling requirement, which can be seen by comparing the control model, Fig. 5, to the physical model, Fig. 10. The relevant physical phenomena include thermal, electrical, optical, and photoelectric effects. The circular, nonlinear

Optics EXPRESS

system of physical equations are derived in the Appendix, yet do not need to be solved for weight control. All of these effects are countered during the feedback control stage which has no modeling requirement.

In the control rules, there is reference to parameters that are fixed regardless of command weight values. Their values must be determined during a calibration phase with a calibration procedure. Table 2 summarizes the parameters involved in control along with calibrated values from a typical device. In this section, we describe the calibration procedure in steps, each including: the procedure, the parameters that are calibrated, any modifications needed for the multichannel case, and the intermediate control rules enabled by that step.

3.1. Common parasitic resistance (multichannel only)

The MRRs share a common ground (GND) trace which has a parasitic resistance. As described in Sec. 7.4, this causes a difference between measured voltage and voltage just across the heaters, which must be accounted for when using >1 channel. We first calibrate the common connection resistance, R_{comm}, with the lasers turned off. R_{comm} is described by a $N \times N$ matrix (Eq. (24)). First, the current is zeroed on all but channel i.

$$I_i = I_{set} \neq 0\,; \quad I_{j\neq i} = 0 \tag{5}$$

and then voltage is measured on all other channels to fill out one row of the common resistance matrix

$$R_{comm,ji} = V_{j,meas}/I_{set} \;\; \forall\, j \tag{6}$$

This is repeated over all i. After this step, the actual heater voltages can be derived from the measured voltages by applying the R_{comm} matrix to the known vector of currents.

3.2. Baseline sweep in current

To assess the electric and thermo-electric properties, the laser is turned off, and the applied current is swept for one channel at a time. The measured voltage is used to calculate applied power and resistance. This relation is fitted with a linear regression to find ambient resistance and the thermo-electric coefficient. In the multi-channel case, current is kept at zero for all other channels. After this step, the parameters needed for the control rule $\langle I \rangle \leftarrow \langle \underline{\mathrm{P}} \rangle$ have been calibrated, enabling further calibration steps to proceed in terms of nominal electrical power.

3.3. Photoresponse peak search

In this step onward, all DFB lasers are turned on. The deviation of voltage away from baseline (i.e. lights-off) voltage is used as an indicator of photoresponse or circulating optical power within the MRR. We perform a Nelder-Mead search [65] to converge on the peak photoresponse occurring at resonance. The calibration parameters for nominal applied power, $\underline{\mathrm{P}}_{res}$, and maximum photovoltage, $\Delta V_{\max}$, are determined by the on-resonance point. In the multi-channel case, this peak search occurs simultaneously for all channels to find the vector of bias powers. After this step, no additional control rules have been made available; however, it is now possible to calculate the value for estimated transmission, $\hat{D}$, using the newly calibrated parameter $\Delta V_{\max}$. $\hat{D}$, defined in Eq. (19), is not a true transmission and could also be referred to as a normalized photoresponse, which is a function of photovoltage.

3.4. Photoresponse HWHM search

To find the width of the photoresponse peak, we perform a binary search between the peak power and a detuned power, looking for a photoresponse that is half of the peak photoresponse (i.e. $\langle \hat{D} \rangle \leftarrow \hat{D}_{\max}/2$). During the binary search, if the photoresponse is greater than the target, the

Optics EXPRESS

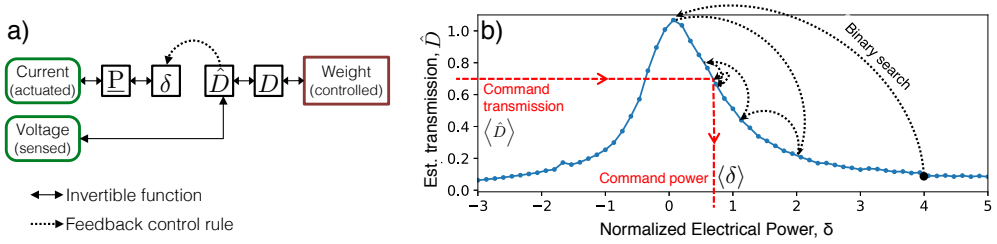

Fig. 5. a) Simplified control model. Feedback control occurs in the domain of δ-$\hat{D}$, which are invertible functions of current and voltage. b) Illustration of the feedback control rule. First, an estimated transmission is requested. Then, the controller performs a binary search for the commanded value over the δ domain. The converged value of δ becomes the commanded value for the thermoelectric control step. Blue, dotted curve: Example measurement of $\hat{D}$ vs. δ. This curve is not measured during calibration because it can shift horizontally with environmental fluctuations.

applied power steps away from resonance – if the photoresponse is below target, the power steps closer to resonance. Every iteration, the magnitude of the power step is halved. The binary search converges efficiently, resulting in an estimate of the half-width at half-maximum power on that side, P_{hwhm}. In the multi-channel case, the searches occur on each channel sequentially while the other channels are held at their approximate resonance point. It is convenient to define a normalized electrical power, δ, as

$$\delta \equiv \frac{\underline{\mathrm{P}} - \underline{\mathrm{P}}_{res}}{P_{hwhm}} \tag{7}$$

so that, at $\delta = \pm 1$, transmission is half of maximum.

The feedback control procedure of $\langle\delta\rangle \leftarrow \left\langle\hat{D}\right\rangle$ is now available. This control procedure consists of a binary search for a target estimated transmission exactly like the HWHM search described above. This binary search is illustrated in Fig 5(b). In the multi-channel case, the binary search for $\hat{D}$ is repeated on each channel twice: first, a rough (10% tolerance) search on each channel is performed sequentially, then, the sequential search is repeated over a small range around the first estimate of δ_i with a finer 1% tolerance. The control rule must be repeated twice because making large changes in the second channel's tuning invalidates the first one due to thermal and electrical cross-talk.

3.5. *Edge transmission correction (optional)*

As discussed in the Appendix, we estimate the relation between transmission of the MRR and voltage deviation from baseline to be quadratic, but this approximation is not exact. For more accurate weighting, we can measure the actual transmission vs. estimated transmission along the filter edge, denoting this correction function as $D = g\left(\hat{D}\right)$. Without this edge correction step, g is assumed to be an identity function. With edge correction, the real transmission, D, is measured directly using the weight decomposition setup described above. A set of binary searches is performed to track the photoresponse to 7 values over the domain $0 < \hat{D} < 1$, thus building an estimate of g. In the multi-channel case, it is not assumed that g is the same for different channels. The set of binary searches occur on each channel sequentially while the other channels are held at their approximate resonance point.

The disadvantage of this step is that it requires direct optical measurements of the weights, plus additional calibration and instrumentation. It thus negates some of the reasons of using feedback control. As a tradeoff, this step gives an increase in weight accuracy, as seen in Sec. 4.

Table 2. **Calibrated parameters used during control**

Name	Symbol	Value	Calibrated during
Common connection resistance (ch. 1→2)	$R_{comm,12}$	120Ω	Step 3.1
Ambient resistance	R_0	2.06kΩ	Step 3.2
Thermoelectric coefficient	α	134 Ω/mW	Step 3.2
Electrical power on resonance	$\underline{P}_{res}$	2.35mW	Step 3.3
Maximum photovoltage	ΔV_{max}	0.26V	Step 3.3
Electrical power offset at half photoresponse	$\underline{P}_{hwhm}$	0.57mW	Step 3.4
Actual vs. estimated transmission	$g(\hat{D})$	function	Step 3.5

It could be rendered obsolete if a better *a priori* estimate of transmission vs. voltage deviation were developed, which is considered in Sec. 5.

4. Results

We perform the above calibration procedure on a two-channel feedback controlled weight bank and then evaluate the accuracy and precision of the following control rule. The evaluator generates a grid of command weight values, which the controller converts to applied currents, as in [52]. The evaluator then measures actual weights through the scope decomposition method. Actual weights are compared to the desired command weights. Performance is quantified in terms of mean deviation from the command weights (a.k.a. accuracy), $\sigma_{accu} = ||\bar{\mu} - \hat{\mu}||$, and their non-repeatable standard deviation around this mean (a.k.a. precision), $\sigma_{prec} = \sqrt{\langle(\mu - \bar{\mu})^2\rangle}$. $\bar{\mu}$ refers to the mean over measurements. Both values can be expressed as a percentage, or a dynamic range DR $= (\mu_{\max} - \mu_{\min})/\sigma$, or as an effective bit resolution: $\log_2(\mathrm{DR})$. Control performance is summarized and compared to prior results in Table 3.

4.1. Single channel control

The single channel control evaluation is shown in Fig. 6 for 21 points over the range of command weight values. The dashed line represents the target weight. Black points are measured weights over 5 trials. The center, red curve is the mean weight value, and the high/low, blue curves show one standard deviation around this mean. The evaluation is repeated at 24°C and 26°C. Laser detuning from as-fabricated MRR resonance, $\lambda_{carrier} - \lambda_0$, is 2.32nm and 2.31nm in these respective cases. At each temperature, calibration is repeated before controlling at that temperature. Using the transmission edge correction in Step 3.5 results in an increase in accuracy from 4.2 bits (5.4% error) to 5.3 bits (2.5%) and precision from 4.8 bits (3.6%) to 5.4 bits (2.4%).

4.2. Multi-channel control

Two-channel weight control results are shown in Fig. 7 over an 11×11 grid and 3 trials. The black grid indicates target weight vectors; red vector lines are mean offset from these targets; blue ellipses represent the two-dimensional standard deviation around these means. Temperature was 26°C, and $\lambda_{carrier} - \lambda_0$ was 2.31nm for each channel. A comparison is made between the case using only the estimate of photoresponse and with the optional transmission edge calibration.

Optics EXPRESS

Table 3. **Accuracy and precision of weight control strategies**

Experiment	Accuracy (bits)	Precision (bits)	Required observations
Single channel			
Feedforward [66]	4.1	5.0	Spectrum, Weight
Feedback	4.2	4.8	Resistance
w/ edge cal.	5.3	5.4	Resistance, Weight
Multi-channel			
Feedforward [52]	4.8	5.0	Spectrum, Weight
Feedback	4.2	5.3	Resistance
w/ edge cal.	5.1	5.5	Resistance, Weight

The accuracy in both cases (4.2 bits (5.4%) without edge cal., 5.1 bits (2.9%) with edge cal.) are very close to those of the one-channel results. Error tends to be worse for negative weight values because these correspond to the more sensitive on-resonance region. The achieved control accuracy is commensurate with state-of-the-art digital weight resolution used in neuromorphic electronics [67,68]. 4 bits + 1 sign bit has been deemed by significant parts of that community to be sufficient for neuromorphic processing [69].

The primary difference in the calibration procedure for multi-channel case is calibrating for common connection resistance, which affects the estimate of voltage across individual heaters. For comparison, we repeated the above evaluation procedure while neglecting common connection resistance (Step 3.1) finding that multi-channel control failed entirely. This indicates that it is both essential and practical to precisely calibrate for the parasitic resistances found in the common ground network.

5. Photoresponse characterization

The relationship between real transmission or weight and the measured photoresponse is important for accurate feedback control. Since current-mode drivers are used, the photoresponse is defined in terms of voltage away from the baseline voltage. We observe a relationship that is approximately quadratic, defining estimated transmission as $\hat{D} \equiv (\Delta V/\Delta V_{\max})^2$ in Eq. (19). To evaluate this estimate, we performed a more detailed characterization of the photoresponse of one device over a range of laser parameters. To the authors' knowledge, a characterization of N-doped heaters such as this has not yet been reported.

Figure 8 shows the effects of input laser power. The laser power is swept from 3mW to 20mW, limited by equipment, and the normalized electronic power, δ, is swept from –1 to 2. The estimated fiber-to-chip coupling efficiency is 28%. The laser detuning is 2.32nm. The transmission is measured with a power meter and the photoresponse is measured with the source-meter. Figure 8(a)–8(b) clearly show a correspondence between voltage change and actual transmission. Figure 8(c) indicates that the on-resonance photoresponse is not proportional to input power, as predicted by the simplified theory in the Appendix. The photoresponse relationship $g : \hat{D} \mapsto D$ is plotted in Fig. 8(d). The black line represents an ideal estimate such that $\hat{D} = D$. The response is nearly correct with slight saturation closer to the resonance point, and it is notably insensitive to laser power.

Optics EXPRESS

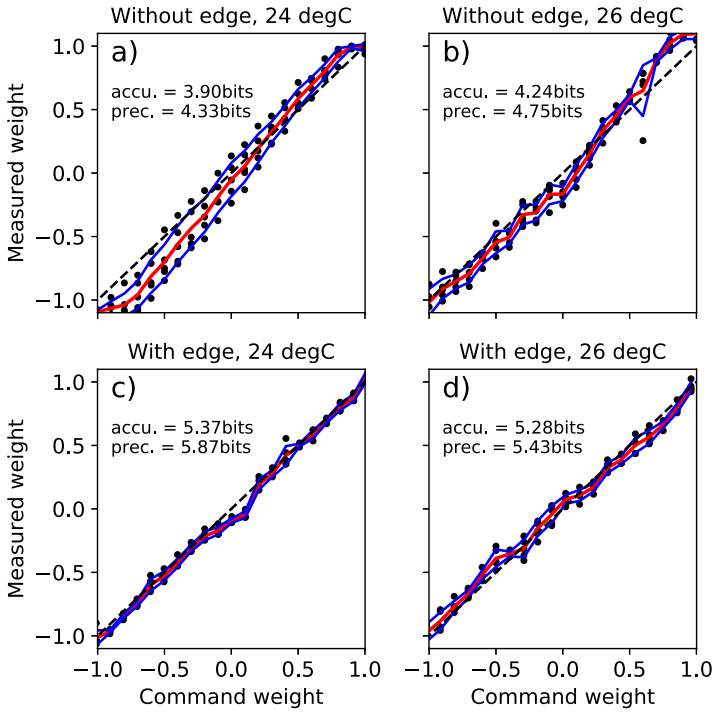

Fig. 6. 1D command-control evaluations of accuracy (accu., center-red lines) and precision (prec., high/low-blue lines) at 24°C and 26°C. The actual measured weight, μ, is plotted against desired command weights, $\hat{\mu}$, and compared to the ideal target (black dashed lines). In (a)–(b), the optical weight edge is not directly measured during calibration (Step 3.5: edge calibration), while, in (c)–(d) the weight edge calibration is performed.

Another characterization is performed by varying the initial wavelength offset of the carrier signal. The laser wavelength away from MRR resonance as-fabricated is swept from 1.85 to 2.32nm. Current is swept from 0 to 1.5mA such that the MRR will tune through the laser wavelength. In Figure 9(a)–9(b), it can be seen that the peak photoresponse and on-resonance transmission are affected by detuning in a nonlinear way. As seen in Figure 9(c), the photoresponse is different for low (left) and high (right) edges of the peak, an effect that gets emphasized at smaller detunings (purple). The photoresponse is larger on the high edge where current is greater. In the laser power sweep in Fig. 8, the detuning was sufficient to not observe the asymmetry.

In both characterizations, the error of the estimate of g can be attributed to an on-resonance transmission that is less than ideal. Supposing a lossless MRR, the decrease in Q factor in Fig. 3 could be explained by temperature-dependent MRR-to-bus couplers; however, this mechanism does not explain the drop in extinction ratio. Due to the heater symmetry, the MRR without internal loss would remain critically coupled to drop 100% power on resonance. Absorption in the heater reduces the peak transmission by breaking this critical coupling condition and/or by absorbing power directly. We can therefore conclude, firstly, that the absorption in the heater is non-negligible compared to the coupling coefficient of the MRR to the WGs and that Eq. (13) is incomplete. In Figure 9, it is also seen that the amount of absorption changes with the applied current to get to resonance. Stronger evidence of bias-dependency is provided by the response being more asymmetric for smaller detunings – where the marginal difference in current between low and high edges is larger. We can therefore conclude, secondly, that

Optics EXPRESS

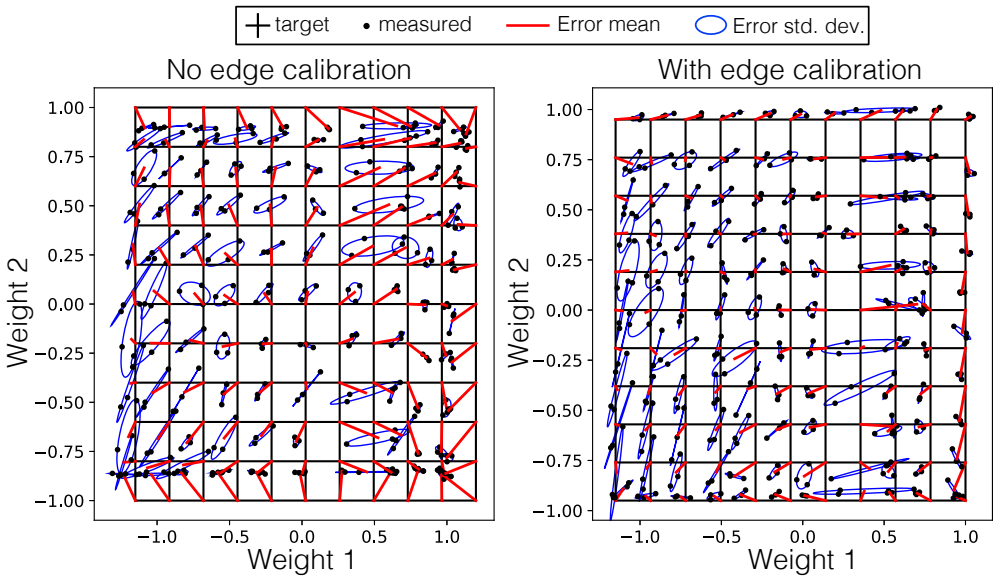

Fig. 7. Evaluation of two-channel command and control, following the format of [52], Fig. 4. Black grid crossings: desired weight vectors. Red arrows: offset between desired and the mean of actual weights over 3 repetitions. Blue ellipses: variance of actual weight values over the repetitions. a) Without the weight edge calibration (Step 3.5), the accuracy is 4.2 bits. b) With edge calibration, the accuracy is 5.1 bits. Accuracy is worse at negative weights because this corresponds to the more sensitive on-resonance point.

Eq. (15) is incomplete, and absorption has other dependencies than just circulating power. This conclusion is corroborated by the nonlinearity of Fig. 8(c). One possible explanation is that a higher bias voltage sweeps the generated photocarriers out of the active region at a faster rate. Another possibility is a temperature-dependent absorption coefficient. Surprisingly, the peak photoresponse and transmission are non-monotonically related to detuning, perhaps a hint that two competing phenomena are being observed.

We did not arrive at a concrete expression for an improved estimate of g as it is affected by the laser power, electrical biasing, temperature, and heater geometry. The estimate performs better for larger initial detunings. The characterizations provided here could be useful for further work towards estimating g. Better estimates of transmission vs. photoresponse would render the filter edge calibration step unnecessary.

6. Discussion

Feedback weight control presents major advantages over feedforward control, especially for larger silicon photonic systems with many resonators. The calibration phase is much simpler and requires fewer measurements. In contrast to past work, no thermal cross-talk calibration is necessary. Furthermore, the control phase is robust to temperature fluctuations very likely to occur outside of the stabilized laboratory setting.

6.1. Sources of temperature fluctuation

Realistic analog photonic networks will very likely contain two significant sources of heat: CMOS controllers and laser neurons. The amount of heat these generate in close proximity to the silicon photonic layer can fluctuate significantly in a way that is difficult to predict on the

Optics EXPRESS

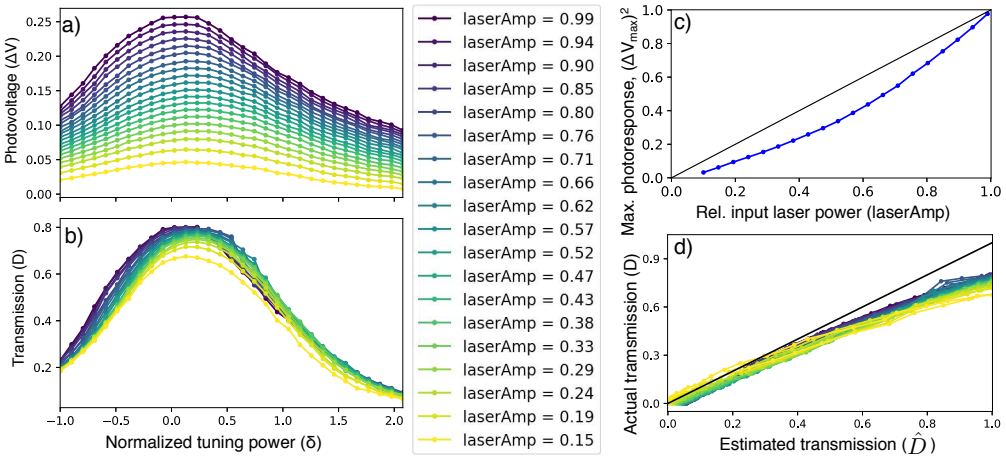

Fig. 8. Saturation characteristic of a N-doped weight. (a-b) A sweep through relative tuning, normalized to HWHM, over a range of input laser powers (input laser powers in legend relative to 20mW maximum). a) Change in voltage away from the nominal value expected in absence of a laser; b) Transmission of the DROP port measured directly by a power meter. c) Peak photoresponse on-resonance as a function of the laser power, where the black line represents proportionality. d) Actual transmission, from (b), plotted against estimated transmission, a function of (a), where the solid black line represents an ideal estimate.

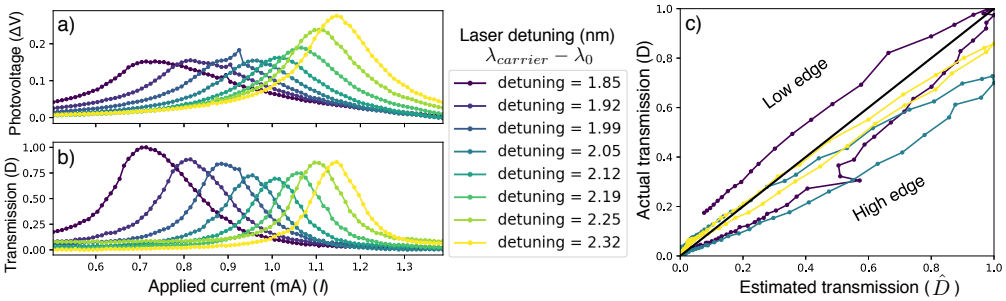

Fig. 9. Transmission and photoresponse for a range of initial laser wavelength detunings. a) Change in measured voltage away from baseline. b) Actual transmission measured by a power meter. c) Actual transmission, D, from (b) plotted against estimated transmission, where the solid black line represents an ideal estimate.

fly. Co-integrated CMOS controllers will become necessary for systems to scale beyond wire bonded I/O count limits. Numerous researchers in the neuromorphic photonics community have reported semiconductor lasers that exhibit neuron-like spiking behavior [70–74]. Spiking laser neurons, proposed by Nahmias et al. in 2013 [75] and reviewed in [76], all generate heat that could potentially vary with activity. In this situation, feedforward weight control techniques relying on complete temperature predictability will be infeasible.

6.2. *Filter edge correction*

Calibration of the transmission edge in terms of actual vs. estimated transmission had a significant impact on control accuracy. This step defeats some of the purposes for feedback control in that

Optics EXPRESS

transmissions must be measured during the calibration phase. A key difference between these measurements and the calibration measurements needed for feedforward control is that only one channel's transmission must be measured at a time. One direction for further work would be performing calibration with a power meter as opposed to scope-based weight decomposition (although decomposition would still be needed to evaluate control accuracy). Another direction would be more accurate *a priori* estimates of the photoresponse function, g, such that edge correction measurements are not needed.

6.3. Control within a network

Prior work argued that online weight control for neuromorphic photonics would be a particular challenge because average optical power levels are affected by activity [66]. A consistent input power is needed to act as a reference level for in-ring sensor response. In the complete silicon photonic neural network shown in Fig. 1(b), it can be seen that MRR modulator neurons stand between the pump lasers and MRR weights. Weight values affect network dynamics including the average transmission of neurons, thus creating a circular, unstable, and non-local dependency between the transmissions of all the weights and of all the modulators. This type of coupling is in fact essential for creating a complex dynamical system capable of information processing.

When using MRR modulator-class neurons, it is always possible to temporarily break this circular dependency by detuning the MRR neurons. This ensures that a consistent power reaches the weight banks regardless of their weight states. At that point, the weights can be appropriately calibrated and configured, after which the photonic neurons would be brought back to resonance with their respective carrier signals. The time to reconfigure weights is much slower than the signal bandwidth, which is typical of neural networks; nevertheless, reconfiguration time is an important metric in some applications. Further work could seek to reduce this time using fast, non-thermal tuning effects and/or optimized control algorithms, perhaps combining prior techniques in lookup-based feedforward calibration with feedback adjustments.

The device pictured in Fig. 2 was originally fabricated to address the issue of varying input power levels – by using 3 MRRs per wavelength, a differential measurement between the total input power and power coupled through the weight could be made. Further work could investigate using the additional sense MRRs when the input power level is unknown, although this appears to be unnecessary with networks of MRR modulator neurons.

6.4. Footprint

Work on continuous transmission control for analog matrix multiplication in silicon photonics has focused on grids of microrings (MRRs) [25, 43] and meshes of Mach-Zehnder interferometers (MZI) [22, 26, 77]. MRR-based weights represent an area savings of more than 10× when compared to MZI-based weights. In this work, the longitudinal MRR pitch was arbitrarily chosen to be 300μm but could be reduced to 50μm accounting for the contact design needed for feedback control, shown in Fig. 2(a). The lateral pitch is limited by the MRR radius and offset between a DROP WG and the THRU WG of the subsequent weight bank. Assuming the radius of 8μm used here and a DROP WG spacing of 5μm results in a lateral pitch of 30μm. For comparison, the length of MZIs is limited by directional coupler length (20μm), WG routing into and away from the coupler (40μm), and thermal phase shifter length (40μm), where the values in parentheses come from [22]. The lateral heater pitch was 80μm, limited by heater width and access WG radius. Each matrix element requires two MZIs leading to a footprint of 200μm × 80μm – 10.7 times the MRR weight footprint of 50μm × 30μm. Feedback control strategies for MZI matrices applying configurable unitary operations have been proposed [78], and a system for demixing a multi-mode input has been demonstrated by Annoni et al. [61]. Incorporating feedback sensors further increase the mesh footprint, for example, the contactless probes used in [61] have a minimum useful length of 50μm [79]. In [25], the authors calculated that a broadcast and weight

network of 25 neurons would consume 106mW and occupy 0.39mm^2 with passive weights. Substituting the larger area of an N-doped weight would increase that area to 0.94mm^2.

7. Conclusion

We have demonstrated continuous, multi-channel feedback control of a MRR weight bank using embedded N-doped photoconductive heaters as sensors. Furthermore, we presented a rigorous characterization of photoresponse for over a range of carrier wavelength offsets and powers.

Controlling MRR filter response is a challenge in all MRR circuits due to fabrication variations and thermal sensitivity. This work exhibits major advantages over prior MRR weight bank control approaches in the form of calibration simplicity, required instrumentation, and control robustness. It is distinct from prior work on MRR feedback control because it shows control over a continuous range of transmission values, rather than tracking a single on-resonance point.

Further work includes developing control procedures that can attain the highest accuracy without direct off-chip transmission measurements, instead employing on-chip detectors or more accurate modeling of the relation between photoresponse and actual transmission. Another direction would be introducing feedback control for two-pole MRR weights, which have substantial impact on channel count and robustness [80]. Electrical I/O is a limiting factor in photonic integrated system scaling, so other further work could investigate co-integrated CMOS controllers capable of performing the necessary calibration and control procedures.

Feedback control renders feasible the problem of controlling large analog networks of microring weights. Microring weight banks present novel opportunities for reconfigurable analog photonic networks. Rapid developments in silicon photonic platforms and the surrounding industry could soon enable large-scale analog photonic systems with applications to new performance domains of machine information processing.

Appendix: Theory and model

The N-doped heater embedded in a MRR with an incoming laser signal contains an interplay of thermal, optical, and photoelectric effects. The calibration/control rules in this work rely on an understanding of these effects, although, unlike a feedforward controller, they do not need to solve the equations to precisely invert the system of equations. The full model is shown in Fig. 10. Both resistance and refractive index change with temperature. Refractive index affects transmission at the laser wavelength. Transmission affects the photoelectric absorption, which in turn affects resistance. Changes in resistance change the applied electrical power at a given applied current. In this section, we derive the relations between underlying physical phenomena since further study of them might yield improved weight control results.

7.1. Thermo-electric effects

The power dissipated in the resistor is well-defined as

$$P = IV = I^2R \quad \text{(Ohm's law, Joule's law)} \tag{8}$$

where I is the applied current – the only independent variable with an ideal current-mode driver – and V is voltage. R is the actual resistance, which depends on temperature and photoelectric absorption. We first consider the heater resistance without any incoming light.

$$R = R_0(1 + \beta\Delta T) \quad \text{(Temperature-dependent resistance)} \tag{9}$$

$$\Delta T = zP + \Delta T_{environmental} \quad \text{(Temperature)} \tag{10}$$

where the parameters are $R_0(\Omega)$: ambient resistance, $\beta(\Omega/K)$: temperature coefficient of resistance, and $\Delta T(K)$: temperature change. The temperature is affected both by dissipated

Optics EXPRESS

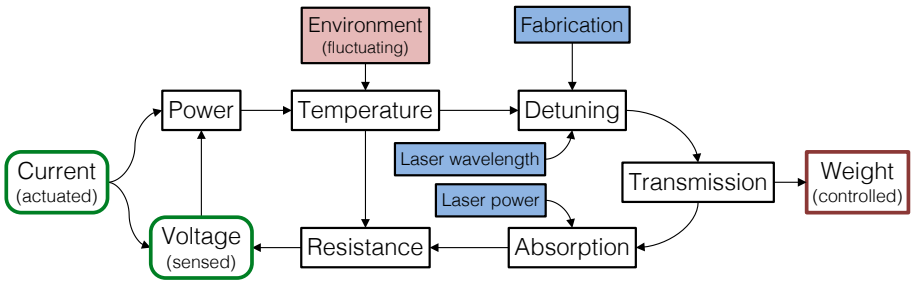

Fig. 10. Physical model of the N-doped heater embedded in a MRR with an incident laser. Red: fluctuating source of variability, Blue: fixed sources of variability. Feedforward control would require high-fidelity modeling of this system, but the feedback control model, shown in Fig. 5, can use a vastly simplified. The effects of varying laser wavelength and power parameters are examined in Sec. 5.

power via z(K/mW): the self-heating coefficient, and by environmental fluctuations. Assuming no optical input and no environmental fluctuation, we can define a baseline of the applied power

$$\underline{\mathrm{R}} \equiv R_0(1 + \alpha P) \tag{11}$$

$$\underline{\mathrm{P}} \equiv \frac{I^2 R_0}{1 - \alpha I^2 R_0} \tag{12}$$

where we use an underbar to indicate the absence of optical input. The parameter $\alpha = \beta z$ is the net change in resistance vs. power in Ω/mW. Already it can be noted that Eq. (12) has an asymptote – this corresponds to thermal runaway that occurs when α is positive and current-mode drivers are used. Equation (12) is used heavily in calibration (Sec. 3) because it maps approximate power to the independent actuation variable, current.

7.2. Transmission and thermo-optic effects

The transmission through the DROP port of a MRR filter is a Lorenzian-like peaked function, $\mathcal{L}$, of the form

$$D = \mathcal{L}\left(\frac{\lambda_r - \lambda_{carrier}}{HWHM_{[\lambda]}}\right) \quad \text{(Resonator transmission)} \tag{13}$$

where D is DROP port transmission and λ_r is the resonance wavelength. The transmission function is a comb with multiple resonances, but we focus only on one resonance order. The parameters are $\lambda_{carrier}$; wavelength of the laser signal, and $HWHM_{[\lambda]}$; half-width half-maximum of the filter peak. The resonance is also affected by temperature:

$$\lambda_r = \lambda_0 + k\Delta T \quad \text{(Thermo-optic resonance shift)} \tag{14}$$

where λ_0 is as-fabricated MRR resonance, k is thermo-optic coefficient in (nm/Kelvin), and ΔT is as in Eq. (10). Just like resistance, the dependent variable λ_r shifts in proportion to dissipated electrical power and is also affected by ambient changes in temperature. The as-fabricated resonance is sensitive to fabrication deviations that are spatially-correlated [81, 82]. For MRRs that are far apart or on different wafers, λ_0 can vary by more than an FSR in the worst-case. When they are nearby, standard deviation in λ_0 can reach 0.35nm [81].

7.3. Photoelectric effects

$$a = uDp_{carrier} \quad \text{(Photo absorption)} \tag{15}$$

Optics EXPRESS

where a is the optical power absorbed within the MRR heater, u is the fraction of light that is absorbed vs. transmitted to DROP port and $p_{carrier}$: optical power of the carrier signal. If we assume that the maximum DROP port transmission is 100%, i.e. $D_{\max} = 1$, then

$$a_{\max} = up_{carrier} \tag{16}$$

$$\frac{D}{D_{\max}} = D = \frac{a}{a_{\max}} \tag{17}$$

where $a_{\max}$ occurs at resonance. This indicates that the transmission can be determined by measuring the electrical photoresponse if the on-resonance photoresponse is also known.

The generated photocarriers reduce the resistance of the N-doped heater; however, this relation is not trivial. Neither change in resistance nor change in current are proportional to a in all cases. For this reason, we describe the electrical impact of photoabsorption as a function. Since we use current as the independent source variable, this function is stated in terms of photovoltage, the dependent measurement variable.

$$V = \underline{\mathrm{V}} - f(a) \quad \text{(Photovoltage)} \tag{18}$$

where $\underline{\mathrm{V}}$ is the baseline voltage without optical input. The function f is monotonically increasing; however, it can vary from MRR to MRR and even within the same MRR with different DFB powers and wavelength offsets. We investigate this relationship in Sec. 5, although do not arrive at a universally accurate formula for f. It is likely that f depends on layout dimensions and semiconductor diffusion and transport quantities.

Through characterization, we observed that the actual transmission is usually proportional to the change in voltage squared, thus we find it convenient to define an approximate transmission

$$\hat{D} \equiv \left(\frac{\Delta V}{\Delta V_{\max}}\right)^2 \tag{19}$$

where $\Delta V = \underline{\mathrm{V}} - V$. $\hat{D}$ is an expression of normalized electrical photoresponse, not a real transmission. Rearranging the above equations, we can replace f with a different function, g, that captures the error of this approximation.

$$D = g(\hat{D}) \tag{20}$$

If the approximation is accurate, then g is the identity $x = y$ function. Controlling the weight value requires inverting g. We take two approaches in the calibration procedure Sec. 3: either relying on the approximation of g^{-1} to be the identity, or directly measuring g and inverting it using interpolation. We find that, in the two-channel case, direct measurement increases accuracy by a factor of two.

Finally, the effective weight is determined by the difference in photocurrents induced in the THRU and DROP port photodiodes which are proportional to the corresponding thru port transmission, T, and DROP port transmission, D. When loss in the MRR is negligible, these transmissions are complementary, resulting in

$$\mu = 1 - 2D \tag{21}$$

7.4. Common connection resistance

The MRRs share a common ground (GND) trace to save on electrical I/O. By using current-mode drivers, the current through each N-doped heater is known exactly; however, since the common trace has a parasitic resistance, the voltage across just N-doped heater number i: $V_{i,heater}$, is

different than the voltage measured by the corresponding source-meter: $V_{i,meas}$. Since continuous calibration relies on an accurate measure of heater voltage, we must account for this difference.

$$V_{GND} \equiv 0 \leq V_{i,comm} \tag{22}$$

$$V_{i,meas} = V_{i,heater} + V_{i,comm} \tag{23}$$

where V_{comm} is the voltage at the junction of the two GND-side traces. In the 2-channel case, shown in Fig. 2(c), the common ground resistance is a scalar. For >2 channels, the common ground tree forms a resistive network. We can use a matrix of resistances, R_{comm}, to describe the relation between the current through all heaters and the common-side voltage of all heaters.

$$V_{i,comm} = \Sigma_j R_{comm,ij} I_j \tag{24}$$

where $R_{comm,ij}$ can have non-zero values depending on the ground network. The matrix of common connection resistances describes the effect that current on channel j has on the voltage observed at channel i. Its values would be difficult to derive from the layout, although it can simply be measured with a straightforward procedure described in calibration Step 3.1.

7.5. Summary

To simulate this device, we would need to specify all of the above parameters. With a feedforward calibration approach, the control rule would need all the parameters and to invert this fairly complex relation. In contrast, for feedback control, the goal is only to estimate transmission based on voltage measurement. In that case, we only need to know the parameters R_0, α, $\Delta V_{\max}$, R_{comm}, and g.

This system of equations is capable of oscillating. When the MRR moves on-resonance, the photoelectric effect reduces the voltage, thereby reducing the actual electrical power. In turn, temperature decreases, blue shifting the resonance. If this shift is sufficient to bring the MRR off-resonance, then voltage will return to its nominal value, thereby red shifting, and so on. The asymmetry of the photoresponse peak in Fig. 5(b) is indicative of the possibility of instability. The left edge (blue shifted from resonance) is steeper, and its slope can increase past vertical, such that no stable solution exists. Oscillation is of course undesirable for weight control. It can be avoided by tuning along the right edge (red shifted from resonance; i.e. electrical powers greater than the nominal resonance power).

Funding

National Science Foundation (NSF) (ECCS 1247298, DGE 1148900).

Acknowledgment

Devices were fabricated at the IME A*STAR foundry in Singapore. Fabrication support was provided via the Natural Sciences and Engineering Research Council of Canada (NSERC) Silicon Electronic-Photonic Integrated Circuits (SiEPIC) Program and the Canadian Microelectronics Corporation (CMC).

References

1. M. Hochberg, N. C. Harris, R. Ding, Y. Zhang, A. Novack, Z. Xuan, and T. Baehr-Jones, "Silicon photonics: The next fabless semiconductor industry," IEEE Solid-State Circuits Magazine **5**, 48–58 (2013).
2. D. Thomson, A. Zilkie, J. E. Bowers, T. Komljenovic, G. T. Reed, L. Vivien, D. Marris-Morini, E. Cassan, L. Virot, J.-M. Fédéli, J.-M. Hartmann, J. H. Schmid, D.-X. Xu, F. Boeuf, P. O'Brien, G. Z. Mashanovich, and M. Nedeljkovic, "Roadmap on silicon photonics," Journal of Optics **18**, 073003 (2016).
3. A.-J. Lim, J. Song, Q. Fang, C. Li, X. Tu, N. Duan, K. K. Chen, R.-C. Tern, and T.-Y. Liow, "Review of silicon photonics foundry efforts," IEEE J. Sel. Top. Quantum Electron. **20**, 405–416 (2014).

Optics EXPRESS

4. J. S. Orcutt, B. Moss, C. Sun, J. Leu, M. Georgas, J. Shainline, E. Zgraggen, H. Li, J. Sun, M. Weaver, S. Urošević, M. Popović, R. J. Ram, and V. Stojanović, "Open foundry platform for high-performance electronic-photonic integration," Opt. Express **20**, 12222–12232 (2012).
5. L. Chrostowski and M. Hochberg, *Silicon Photonics Design: From Devices to Systems* (Cambridge University, 2015).
6. R. W. Keyes, "Optical logic-in the light of computer technology," Optica Acta **32**, 525–535 (1985).
7. D. Brunner and I. Fischer, "Reconfigurable semiconductor laser networks based on diffractive coupling," Optics letters **40**, 3854–3857 (2015).
8. D. Psaltis and Y. Quio, "Optical neural networks," Opt. Photon. News **1**, 17–21 (1990).
9. J. W. Goodman, A. R. Dias, and L. M. Woody, "Fully parallel, high-speed incoherent optical method for performing discrete fourier transforms," Opt. Lett. **2**, 1–3 (1978).
10. P. Asthana, G. P. Nordin, J. Armand R. Tanguay, and B. K. Jenkins, "Analysis of weighted fan-out/fan-in volume holographic optical interconnections," Appl. Opt. **32**, 1441–1469 (1993).
11. A. J. Seeds and K. J. Williams, "Microwave photonics," J. Lightw. Technol. **24**, 4628–4641 (2006).
12. D. Marpaung, C. Roeloffzen, R. Heideman, A. Leinse, S. Sales, and J. Capmany, "Integrated microwave photonics," Laser Photonics Rev. **7**, 506–538 (2013).
13. Y. Liu, A. Choudhary, D. Marpaung, and B. J. Eggleton, "Gigahertz optical tuning of an on-chip radio frequency photonic delay line," Optica **4**, 418–423 (2017).
14. M. P. Chang, N. Wang, B. Wu, and P. R. Prucnal, "A simultaneous variable optical weight and delay in a semiconductor optical amplifier for microwave photonics," J. Lightw. Technol. **33**, 2120–2126 (2015).
15. D. Marpaung, "High dynamic range analog photonic links: Design and implementation," Ph.D. thesis, University of Twente (2009).
16. J. Chiles, S. Buckley, N. Nader, S. W. Nam, R. P. Mirin, and J. M. Shainline, "Multi-planar amorphous silicon photonics with compact interplanar couplers, cross talk mitigation, and low crossing loss," APL Photonics **2**, 116101 (2017).
17. A. M. Weiner, "Ultrafast optical pulse shaping: A tutorial review," Optics Communications **284**, 3669 – 3692 (2011). Special Issue on Optical Pulse Shaping, Arbitrary Waveform Generation, and Pulse Characterization.
18. C. Sima, J. C. Gates, H. L. Rogers, P. L. Mennea, C. Holmes, M. N. Zervas, and P. G. R. Smith, "Phase controlled integrated interferometric single-sideband filter based on planar bragg gratings implementing photonic hilbert transform," Opt. Lett. **38**, 727–729 (2013).
19. J. Wang, H. Shen, L. Fan, R. Wu, B. Niu, L. T. Varghese, Y. Xuan, D. E. Leaird, X. Wang, F. Gan, A. M. Weiner, and M. Qi, "Reconfigurable radio-frequency arbitrary waveforms synthesized in a silicon photonic chip," Nat. Commun. **6**, 5957 (2015).
20. D. Pérez, I. Gasulla, L. Crudgington, D. J. Thomson, A. Z. Khokhar, K. Li, W. Cao, G. Z. Mashanovich, and J. Capmany, "Multipurpose silicon photonics signal processor core," Nat. Commun. **8**, 636 (2017).
21. W. Liu, M. Li, R. S. Guzzon, E. J. Norberg, J. S. Parker, M. Lu, L. A. Coldren, and J. Yao, "A fully reconfigurable photonic integrated signal processor," Nat. Photon. **10**, 190–195 (2016).
22. N. C. Harris, D. Bunandar, M. Pant, G. R. Steinbrecher, J. Mower, M. Prabhu, T. Baehr-Jones, M. Hochberg, and D. Englund, "Large-scale quantum photonic circuits in silicon," Nanophotonics **5**, 456 (2016).
23. P. R. Prucnal and B. J. Shastri, *Neuromorphic Photonics* (CRC Press, 2017).
24. B. J. Shastri, A. N. Tait, T. F. de Lima, M. A. Nahmias, H.-T. Peng, and P. R. Prucnal, "Principles of Neuromorphic Photonics," arXiv:1801.00016 (2018).
25. A. N. Tait, T. F. de Lima, E. Zhou, A. X. Wu, M. A. Nahmias, B. J. Shastri, and P. R. Prucnal, "Neuromorphic photonic networks using silicon photonic weight banks," Sci. Rep. **7**, 7430 (2017).
26. Y. Shen, N. C. Harris, S. Skirlo, M. Prabhu, T. Baehr-Jones, M. Hochberg, X. Sun, S. Zhao, H. Larochelle, D. Englund, and M. Soljačić, "Deep learning with coherent nanophotonic circuits," Nat. Photon. **11**, 441–446 (2017).
27. J. M. Shainline, S. M. Buckley, R. P. Mirin, and S. W. Nam, "Superconducting optoelectronic circuits for neuromorphic computing," Phys. Rev. Applied **7**, 034013 (2017).
28. C. D. Schuman, J. S. Plank, G. S. Rose, G. Chakma, A. Wyer, G. Bruer, and N. Laanait, "A programming framework for neuromorphic systems with emerging technologies," in "Proceedings of the 4th ACM International Conference on Nanoscale Computing and Communication," (ACM, 2017), pp. 15:1–15:7.
29. T. Ferreira de Lima, B. J. Shastri, A. N. Tait, M. A. Nahmias, and P. R. Prucnal, "Progress in neuromorphic photonics," Nanophotonics **6** (2017).
30. K. Vandoorne, P. Mechet, T. Van Vaerenbergh, M. Fiers, G. Morthier, D. Verstraeten, B. Schrauwen, J. Dambre, and P. Bienstman, "Experimental demonstration of reservoir computing on a silicon photonics chip," Nat. Commun. **5** (2014).
31. K. Vandoorne, W. Dierckx, B. Schrauwen, D. Verstraeten, R. Baets, P. Bienstman, and J. V. Campenhout, "Toward optical signal processing using photonic reservoir computing," Opt. Express **16**, 11182–11192 (2008).
32. C. Mesaritakis, V. Papataxiarhis, and D. Syvridis, "Micro ring resonators as building blocks for an all-optical high-speed reservoir-computing bit-pattern-recognition system," J. Opt. Soc. Am. B **30**, 3048–3055 (2013).
33. M. C. Soriano, S. Ortín, D. Brunner, L. Larger, C. R. Mirasso, I. Fischer, and L. Pesquera, "Optoelectronic reservoir computing: tackling noise-induced performance degradation," Opt. Express **21**, 12–20 (2013).
34. F. D. L. Coarer, M. Sciamanna, A. Katumba, M. Freiberger, J. Dambre, P. Bienstman, and D. Rontani, "All-optical reservoir computing on a photonic chip using silicon-based ring resonators," IEEE Journal of Selected Topics in

Optics EXPRESS

Quantum Electronics **24**, 1–8 (2018).
35. A. N. Tait, A. X. Wu, T. Ferreira de Lima, E. Zhou, B. J. Shastri, M. A. Nahmias, and P. R. Prucnal, "Microring weight banks," IEEE J. Sel. Top. Quantum Electron. **22** (2016).
36. J. W. Goodman, "Fan-in and fan-out with optical interconnections," Optica Acta: International Journal of Optics **32**, 1489–1496 (1985).
37. R. Genov and G. Cauwenberghs, "Charge-mode parallel architecture for vector-matrix multiplication," IEEE Trans. Circuits Syst. II, Analog Digit. Signal Process.(1993–2003) **48**, 930–936 (2001).
38. G. Cowan, R. Melville, and Y. Tsividis, "A VLSI analog computer/digital computer accelerator," IEEE J. Solid-State Circuits **41**, 42–53 (2006).
39. J. Binas, D. Neil, G. Indiveri, S.-C. Liu, and M. Pfeiffer, "Precise deep neural network computation on imprecise low-power analog hardware," arXiv preprint arXiv:1606.07786 (2016).
40. J. J. Ackert, J. K. Doylend, D. F. Logan, P. E. Jessop, R. Vafaei, L. Chrostowski, and A. P. Knights, "Defect-mediated resonance shift of silicon-on-insulator racetrack resonators," Opt. Express **19**, 11969–11976 (2011).
41. A. H. Atabaki, A. A. Eftekhar, M. Askari, and A. Adibi, "Accurate post-fabrication trimming of ultra-compact resonators on silicon," Opt. Express **21**, 14139–14145 (2013).
42. P. Alipour, A. H. Atabaki, M. Askari, A. Adibi, and A. A. Eftekhar, "Robust postfabrication trimming of ultracompact resonators on silicon on insulator with relaxed requirements on resolution and alignment," Opt. Lett. **40**, 4476–4479 (2015).
43. A. N. Tait, M. A. Nahmias, B. J. Shastri, and P. R. Prucnal, "Broadcast and weight: An integrated network for scalable photonic spike processing," J. Lightw. Technol. **32**, 4029–4041 (2014).
44. J. M. Shainline, S. M. Buckley, A. N. McCaughan, M. Castellanos-Beltran, C. A. Donnelly, M. L. Schneider, R. P. Mirin, and S. W. Nam, "Superconducting Optoelectronic Neurons II: Receiver Circuits," arXiv preprint arXiv:1805.02599 (2018).
45. J. M. Shainline, A. N. McCaughan, S. M. Buckley, R. P. Mirin, and S. W. Nam, "Superconducting Optoelectronic Neurons IV: Transmitter Circuits," arXiv preprint arXiv:1805.01941 (2018).
46. H. T. Peng, M. A. Nahmias, T. F. de Lima, A. N. Tait, B. J. Shastri, and P. Prucnal, "Neuromorphic photonic integrated circuits," IEEE Journal of Selected Topics in Quantum Electronics pp. 1–1 (2018).
47. K. Nozaki, S. Matsuo, T. Fujii, K. Takeda, E. Kuramochi, A. Shinya, and M. Notomi, "Ultracompact O-E-O converter based on fF-capacitance nanophotonic integration," in "Conference on Lasers and Electro-Optics," (Optical Society of America, 2018), p. SF3A.3.
48. V. K. Narayana, S. Sun, A.-H. A. Badawy, V. J. Sorger, and T. El-Ghazawi, "MorphoNoC: Exploring the design space of a configurable hybrid NoC using nanophotonics," Microprocessors and Microsystems (2017).
49. Q. Xu and R. Soref, "Reconfigurable optical directed-logic circuits using microresonator-based optical switches," Opt. Express **19**, 5244–5259 (2011).
50. T. Ferreira de Lima, A. N. Tait, M. A. Nahmias, B. J. Shastri, and P. R. Prucnal, "Scalable wideband principal component analysis via microwave photonics," IEEE Photonics Journal **8**, 1–9 (2016).
51. A. N. Tait, T. F. de Lima, P. Y. Ma, M. P. Chang, M. A. Nahmias, B. J. Shastri, P. Mittal, and P. R. Prucnal, "Blind source separation in the physical layer," in "52nd Annual Conference on Information Sciences and Systems (CISS)," (IEEE Information Theory Society, 2018), pp. 1–6.
52. A. N. Tait, T. Ferreira de Lima, M. A. Nahmias, B. J. Shastri, and P. R. Prucnal, "Multi-channel control for microring weight banks," Opt. Express **24**, 8895–8906 (2016).
53. H. Jayatilleka, K. Murray, M. Ángel Guillén-Torres, M. Caverley, R. Hu, N. A. F. Jaeger, L. Chrostowski, and S. Shekhar, "Wavelength tuning and stabilization of microring-based filters using silicon in-resonator photoconductive heaters," Opt. Express **23**, 25084–25097 (2015).
54. J. C. C. Mak, W. D. Sacher, T. Xue, J. C. Mikkelsen, Z. Yong, and J. K. S. Poon, "Automatic resonance alignment of high-order microring filters," IEEE Journal of Quantum Electronics **51**, 1–11 (2015).
55. C. T. DeRose, M. R. Watts, D. C. Trotter, D. L. Luck, G. N. Nielson, and R. W. Young, "Silicon microring modulator with integrated heater and temperature sensor for thermal control," in "Conference on Lasers and Electro-Optics," (Optical Society of America, 2010), p. CThJ3.
56. Y. Li and A. W. Poon, "Active resonance wavelength stabilization for silicon microring resonators with an in-resonator defect-state-absorption-based photodetector," Opt. Express **23**, 360–372 (2015).
57. S. Grillanda, M. Carminati, F. Morichetti, P. Ciccarella, A. Annoni, G. Ferrari, M. Strain, M. Sorel, M. Sampietro, and A. Melloni, "Non-invasive monitoring and control in silicon photonics using cmos integrated electronics," Optica **1**, 129–136 (2014).
58. W. A. Zortman, A. L. Lentine, D. C. Trotter, and M. R. Watts, "Bit-error-rate monitoring for active wavelength control of resonant modulators," IEEE Micro **33**, 42–52 (2013).
59. J. A. Cox, A. L. Lentine, D. C. Trotter, and A. L. Starbuck, "Control of integrated micro-resonator wavelength via balanced homodyne locking," Opt. Express **22**, 11279–11289 (2014).
60. D. A. B. Miller, "Self-aligning universal beam coupler," Opt. Express **21**, 6360–6370 (2013).
61. A. Annoni, E. Guglielmi, M. Carminati, G. Ferrari, M. Sampietro, D. A. Miller, A. Melloni, and F. Morichetti, "Unscrambling light—automatically undoing strong mixing between modes," Light: Science & Applications **6**, e17110 EP – (2017).
62. A. N. Tait, J. Chang, B. J. Shastri, M. A. Nahmias, and P. R. Prucnal, "Demonstration of WDM weighted addition for

Optics EXPRESS

principal component analysis," Opt. Express **23**, 12758–12765 (2015).
63. T. Baehr-Jones, R. Ding, A. Ayazi, T. Pinguet, M. Streshinsky, N. Harris, J. Li, L. He, M. Gould, Y. Zhang, A. E.-J. Lim, T.-Y. Liow, S. H.-G. Teo, G.-Q. Lo, and M. Hochberg, "A 25 Gb/s Silicon Photonics Platform," arXiv preprint arXiv:1203.0767 (2012).
64. Y. Wang, J. Flueckiger, C. Lin, and L. Chrostowski, "Universal grating coupler design," in "Proc. SPIE 8915, 89150Y," (2013).
65. J. Nelder and R. Mead, "A simplex method for function minimization," Computer Journal **7**, 303–318 (1965).
66. A. Tait, T. Ferreira de Lima, M. Nahmias, B. Shastri, and P. Prucnal, "Continuous calibration of microring weights for analog optical networks," IEEE Photon. Techol. Lett. **28**, 887–890 (2016).
67. S. Friedmann, N. Frémaux, J. Schemmel, W. Gerstner, and K. Meier, "Reward-based learning under hardware constraints - using a RISC processor embedded in a neuromorphic substrate," Front. Neurosci. **7** (2013).
68. F. Akopyan, J. Sawada, A. Cassidy, R. Alvarez-Icaza, J. Arthur, P. Merolla, N. Imam, Y. Nakamura, P. Datta, G.-J. Nam, B. Taba, M. Beakes, B. Brezzo, J. Kuang, R. Manohar, W. Risk, B. Jackson, and D. Modha, "TrueNorth: Design and tool flow of a 65 mW 1 million neuron programmable neurosynaptic chip," IEEE Trans. Comput. Aided Des. Integr. Circuits Syst. **34**, 1537–1557 (2015).
69. T. Pfeil, T. Potjans, S. Schrader, W. Potjans, J. Schemmel, M. Diesmann, and K. Meier, "Is a 4-bit synaptic weight resolution enough? – constraints on enabling spike-timing dependent plasticity in neuromorphic hardware," Frontiers in Neuroscience **6**, 90 (2012).
70. F. Selmi, R. Braive, G. Beaudoin, I. Sagnes, R. Kuszelewicz, and S. Barbay, "Relative refractory period in an excitable semiconductor laser," Phys. Rev. Lett. **112**, 183902 (2014).
71. B. J. Shastri, M. A. Nahmias, A. N. Tait, A. W. Rodriguez, B. Wu, and P. R. Prucnal, "Spike processing with a graphene excitable laser," Sci. Rep. **6**, 19126 EP – (2016).
72. B. Romeira, R. Avó, J. M. L. Figueiredo, S. Barland, and J. Javaloyes, "Regenerative memory in time-delayed neuromorphic photonic resonators," Sci. Rep. **6**, 19510 EP – (2016).
73. T. Deng, J. Robertson, and A. Hurtado, "Controlled propagation of spiking dynamics in vertical-cavity surface-emitting lasers: Towards neuromorphic photonic networks," IEEE Journal of Selected Topics in Quantum Electronics **23**, 1–8 (2017).
74. S. Buckley, J. Chiles, A. N. McCaughan, G. Moody, K. L. Silverman, M. J. Stevens, R. P. Mirin, S. W. Nam, and J. M. Shainline, "All-silicon light-emitting diodes waveguide-integrated with superconducting single-photon detectors," Applied Physics Letters **111**, 141101 (2017).
75. M. A. Nahmias, B. J. Shastri, A. N. Tait, and P. R. Prucnal, "A leaky integrate-and-fire laser neuron for ultrafast cognitive computing," IEEE J. Sel. Top. Quantum Electron. **19**, 1–12 (2013).
76. P. R. Prucnal, B. J. Shastri, T. Ferreira de Lima, M. A. Nahmias, and A. N. Tait, "Recent progress in semiconductor excitable lasers for photonic spike processing," Adv. Opt. Photon. **8**, 228–299 (2016).
77. J. Carolan, C. Harrold, C. Sparrow, E. Martín-López, N. J. Russell, J. W. Silverstone, P. J. Shadbolt, N. Matsuda, M. Oguma, M. Itoh, G. D. Marshall, M. G. Thompson, J. C. F. Matthews, T. Hashimoto, J. L. O'Brien, and A. Laing, "Universal linear optics," Science **349**, 711 (2015).
78. D. A. B. Miller, "Perfect optics with imperfect components," Optica **2**, 747–750 (2015).
79. M. Carminati, A. Annoni, F. Morichetti, E. Guglielmi, G. Ferrari, D. O. M. de Aguiar, A. Melloni, and M. Sampietro, "Design guidelines for contactless integrated photonic probes in dense photonic circuits," J. Lightw. Technol. **35**, 3042–3049 (2017).
80. A. N. Tait, A. X. Wu, T. F. de Lima, M. A. Nahmias, B. J. Shastri, and P. R. Prucnal, "Two-pole microring weight banks," Opt. Lett. **43**, 2276–2279 (2018).
81. L. Chrostowski, X. Wang, J. Flueckiger, Y. Wu, Y. Wang, and S. T. Fard, "Impact of fabrication non-uniformity on chip-scale silicon photonic integrated circuits," in "Optical Fiber Communication Conference," (OSA, 2014), p. Th2A.37.
82. Z. Lu, J. Jhoja, J. Klein, X. Wang, A. Liu, J. Flueckiger, J. Pond, and L. Chrostowski, "Performance prediction for silicon photonics integrated circuits with layout-dependent correlated manufacturing variability," Opt. Express **25**, 9712–9733 (2017).